Direct Fusion Drive for Interstellar Exploration

S.A. Cohen[1*], C. Swanson[1], N. McGreivy[1], A. Raja[3], E. Evans[1], P. Jandovitz[1], M. Khodak[3], Gary Pajer[2], T.D. Rognlien[4], Stephanie Thomas[2], and Michael Paluszek[2]
[1] Princeton Plasma Physics Laboratory, Princeton NJ, USA
[2] Princeton Satellite Systems, Plainsboro, NJ, USA
[3] Princeton University, Princeton, NJ, USA
[4]Lawrence Livermore National Laboratory, Livermore, CA, USA

Abstract

The Direct Fusion Drive rocket engine (DFD), based on the Princeton Plasma Physics Laboratory's Princeton Field Reversed Configuration machine, has the potential to propel spacecraft to interstellar space and to nearby solar systems. This paper discusses a design for a starship that would be well suited to a variety of solar system and interstellar missions. DFD employs a unique plasma heating system to produce nuclear fusion engines in the range of 1 to 10 MW, ideal for human solar-system exploration, robotic solar-system missions, and interstellar missions. This paper gives an overview of the physics of the engine. Its innovative radiofrequency (RF) plasma heating system and the fuel choice are explained. The thrust augmentation method is described along with results of multi-fluid simulations that give an envelope of expected thrust and specific impulse. The power balance is described and the subsystems needed to support the fusion core are reviewed. The paper gives the latest results for the system design of the engine, including just-completed work done under a NASA NIAC study. A mass budget is presented for the subsystems. The paper then presents potential interstellar missions. The first are flyby missions. One is the proposed 550-AU mission that would use the Sun as a gravitational lens for exoplanet research. This mission can be done without a deceleration phase. Next, flyby missions – requiring major technological advances – to the nearest star are described. Finally we sketch a mission to orbit a planet in either the Alpha Centauri A or Alpha Centauri B systems. The mission analyses include a communications system link budget. DFD can operate in an electric-power-only mode, allowing a large fraction of the fusion power to be used for the payload and communications, enhancing the scientific return. All of the missions start in low earth orbit.

Keywords: Nuclear Fusion, Propulsion, Gravity Lens, 550 AU, Exoplanets, Alpha-Centauri, Interstellar

Nomenclature

B = magnetic field
β = ratio of plasma pressure to magnetic-field energy density
c = speed of light
c_s = ion sound speed
E = ratio of plasma FRC plasma core length to diameter
γ_{LH} = Lower-hybrid drift instability growth rate
I_p = plasma current
I_{sp} = specific impulse
MT = metric ton, 10^3 kg
q = plasma safety factor
r_s = FRC core plasma radius
s = $0.3\, r_s/\rho_i$
S* = $r_s\, \omega_{pi}/c$
T_h = Thrust
τ_A = Alfvén time ~ r_sE/c_s
ω_{pi} = ion plasma frequency

1. Introduction

The idea to use fusion power for spacecraft propulsion has a long history,[1,2] with its support arising from the high energy density of the fuel and the high velocity of the fusion products. Early proponents of fusion rockets that provided steady – rather than pulsed or explosive – propulsion based their designs on the fusion devices that were then in vogue, tokamaks,[3,4] mirror machines[5] and levitated dipoles.[6] The experimental results of that period in fusion history indicated that the plasma's anomalous transport, meaning poor plasma energy confinement, and instability would necessitate low β, D-T burning, large and powerful machines, many meters in diameter, producing over a gigawatt in power and requiring a meter or more of neutron shielding. Such large

---

*Corresponding author, scohen@PPPL.gov

and massive devices could not be launched fully assembled; upwards of 100 launch vehicles would be needed. Such daunting and expensive proposals never proceeded beyond the conceptual stage.

Recently, new designs of fusion devices, bolstered by experimental successes on prototypes, have raised optimism for the prospect of considerably smaller fusion-powered rockets that are far lighter, less radioactive, and less costly. Commensurate with their reduced size, these rocket engines would produce *only* megawatts of power,[7] nevertheless ample for a wide variety of missions in the solar system and beyond. The common feature of these rockets is the geometry of the magnetic field that confines the plasma. The “family name” for these fusion-reactor designs is field-reversed configuration (FRC), a label derived from the original plasma-formation method, not the shape of the field, as commonly thought.

Importantly, FRCs have more than 10x higher β than tokamak devices, the leading contender for terrestrial fusion power production. The high β, coupled with the FRC’s quasi-linear geometry, reduce the required peak magnetic field by about a factor of 3 compared to a tokamak’s. Lighter weight magnets are possible, important for spacecraft. The higher β also allows the use of so-called *aneutronic* fuels, *e.g.,* D-^{3}He*,* whose main reaction produces far fewer neutrons than D-T fusion. Accordingly, less shielding (mass) is required. One member of the FRC family – the inductively driven, liner-compression Pulsed-High-Density (PHD) device – was designed to operate in a pulsed mode with D-T, producing an average power of 70 MW. Another FRC family member is the Star Thrust Experiment (STX),[8] a 1-m plasma radius design, formed and heated by an RF technique called rotating magnetic fields[9,10] (RMF). An STX rocket engine was predicted to be able to produce steady propulsion at a power level near ½ MW/m of length.

In this paper we describe a 3rd member of the FRC family, the D-^{3}He-fueled Direct Fusion Drive (DFD) rocket engine.[11] Similar to STX in employing RMF, the DFD differs in major ways, ones that would result in a more practical rocket engine. Important differences are: 1) the DFD RMF method has different *symmetry*[12] (odd-parity *versus* even parity*,* $\mathrm{RMF_o}$ *vs* $\mathrm{RMF_e}$), providing improved energy confinement hence allowing plasmas with 4-8 times smaller linear dimensions and 100-400x smaller volume and mass; 2) The smaller radius DFD plasma is far more stable than the larger STX plasma; 3) the smaller radius of the DFD plasma allows a method to improve the properties of the rocket exhaust, with specific impulse, I_{sp}, to 2×10^4 s (and beyond) and thrust, T_h, to 10 N/MW; 4) DFD operation reduces neutron wall fluxes more than a factor of 1000 compared to D-T devices, thereby reducing neutron shielding thickness by a factor of 10 and increasing engine lifetime; and 5) increased attention to the engineering details of the complete rocket engine, such as improving energy-recovery systems, raising specific power, and optimizing plasma heating and fueling systems.

In section 2 of this paper we describe the physics of the DFD’s fusion core, explaining how the novel $\mathrm{RMF_o}$ method improves energy confinement, current drive, plasma heating, and plasma stability. Section 3 described the choice of fuel, the neutron production rate, and the power balance. Section 4 describes how the energy in fusion products produced in the core is converted into directed momentum for propulsion. Section 5 describes two missions relevant to interstellar exploration.

2. The DFD rocket engine core

The region where abundant fusion reactions take place is the high temperature (*ca.* 100 keV), moderate density (*ca.* 5×10^{14} cm^{-3}) plasma region named the core. For the FRC, this region is inside a magnetic separatrix, an *imaginary* closed surface that demarcates *open* magnetic-field lines, those that leave the device, from *closed* magnetic-field lines, ones that stay fully inside the device, see Figure 1. The open field-line region is also called the scrape-off layer, SOL.

To form the closed magnetic-field lines, a strong plasma current is needed, perpendicular to the FRC’s magnetic field. On axis, the direction of the magnetic field created by the plasma current, I_p, is opposite to that of the open field lines which are created by external coils. If the axes of the two fields are not exactly parallel, MHD theory[13] predicts that the configuration will strongly tilt and destroy itself. In the following subsection we shall describe how $\mathrm{RMF_o}$ generates the current and heats the plasma ions and electrons in such a way as to allow smaller devices with excellent stability, not susceptible to the tilt mode.

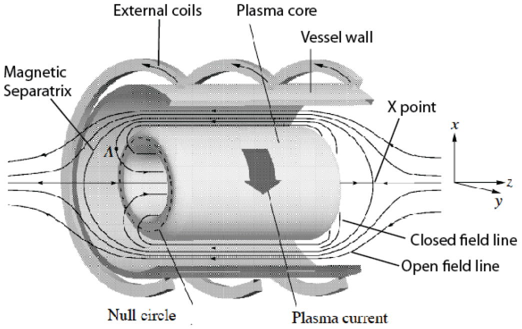

Figure 1. FRC sketch, adapted from Ref. 26.

---

*Corresponding author, scohen@PPPL.gov

2.1. Macro-stability

MHD theory has shown itself to be accurate in predicting the stability of plasmas that are fluid-like.[14] Fluid-like plasmas are prone to several classes of instabilities. Criteria that determine whether a magnetized plasma is fluid-like are collisionality and the ratio of particle gyro-radii to machine size. Highly collisional, that is, cold and dense, plasmas are fluid-like. Plasmas where the ion gyro-radii, ρ_i, are small compared to the plasma radius, r_s, are likely to be fluid-like. For an FRC, the size criterion is defined by two nearly equivalent dimensionless parameters: $s \cong 0.3\, r_s/\rho_i$ and $S^* \equiv r_s \omega_{pi}/c$, where ω_{pi} is the ion plasma frequency and c the speed of light.[15] By choosing a small, high-temperature FRC, neither fluid criterion is satisfied and the plasma is said to be *kinetic* rather than fluid-like. Why a kinetic plasma is stable against the tilt mode can be understood by considering the axis-encircling orbit of a single charged particle in a magnetic field, a stand-in for a hot plasma. An axial push to the particle, in an attempt to tilt its axis, causes the particle to translate along **B**, not to tip over. No tilt occurs. More complicated explanations can be extracted from Steinhauer's review.[16] It should be noted that several FRCs[17,18,19,20] have achieved stable plasmas for durations 10^3 to 10^5 times longer than predicted by MHD theory, the Alfven time, τ_A. (Stability is predicted[15] for $S^*/E < 3$.) The plasma durations were limited by power supply capabilities not instabilities.

We now address how RMF_o heats particles and allows the size of the FRC to be relatively small.

2.2. Confinement

There are several reasons why energy confinement in FRCs can be good, that is, better than in tokamaks. We first discuss how to keep the FRC confinement from becoming poor!

The net magnetic field caused by the external coils and the plasma current creates a nested set of closed field lines inside a separatrix; each closed field line circles the plasma current *once* poloidally before closing on itself. Closed field lines are good for confinement since they encourage charged particles to stay within the device. Open field lines allow particles and their energy to flow out of the device, *i.e.,* confinement is poorer for open field lines. The addition of RMF_e to an FRC causes the field lines to open, see figure 2, while application of RMF_o maintains the closure of field lines, figure 3. One explanation is that the FRC, by itself, is of odd parity.[21] Mixing parities, such as by adding RMF_e, causes all of an FRC's field lines to open, hence confinement to degrade. One experimental team[22] has compared even and odd-parity electron heating on the same device and found a factor of 4 improvement in the energy confinement time. Another team[19] achieved 5 to 10-fold increases in electron temperature, T_e, with RMF_o compared to other machines, *e.g.,* Ref. 9, of the same size and heating power operating with RMF_e.

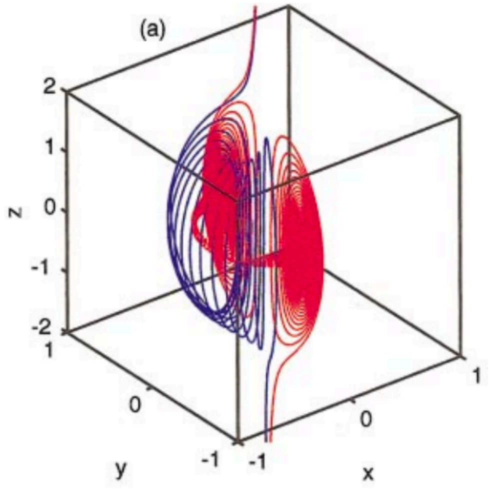

Figure 2. A very small-amplitude (B_t = .005), uniform, transverse magnetic field (even parity) is added to a Solov'ev FRC with $B_0 = 1$. Two field lines are mapped. Though both field lines are long, they are clearly open. This FRC's major axis is vertical.[12]

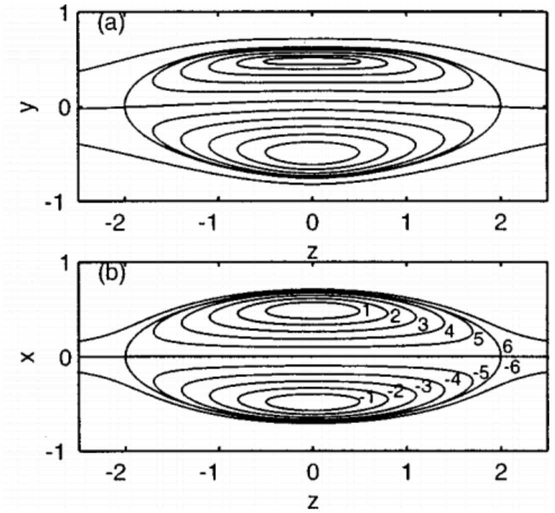

Figure 3. Magnetic field lines when a larger amplitude odd-parity magnetic field, $B_t = 0.04$, is added to a Solov'ev FRC. a) Closed field lines in the y – z plane show expansion and contraction but remain closed. b) Projection of field lines originally in the x – z plane onto that plane show little change in shape. This FRC's major axis is horizontal.[12]

---

*Corresponding author, scohen@PPPL.gov

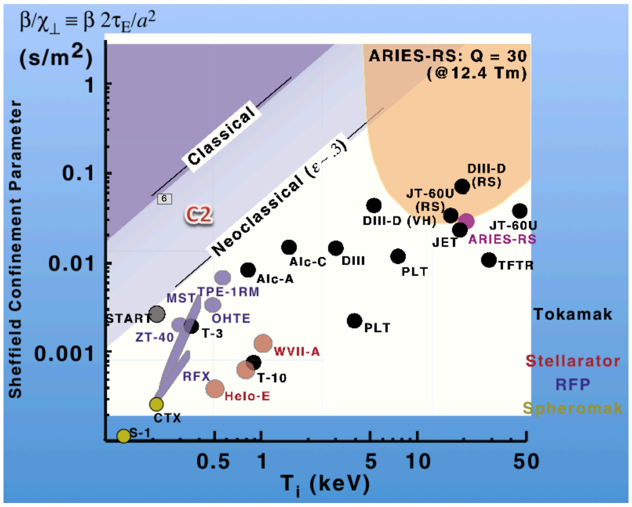

Figure 4. Confinement quality *vs* ion temperature, T_i. The TriAlpha C-2 FRC device has shown better confinement quality, β/χ, than tokamaks. (Adapted from Sheffield,[23] by Mauel and Kesner.)

Neoclassical theory[24] predicts that energy losses scale as $(1 + q^2)$. For tokamaks $q \geq 3$ while for pure FRCs $q = 0$. Accordingly, FRCs should have about 10x better confinement. Sheffield prepared a survey of confinement quality in tokamaks which Kesner and Mauel updated; the results are shown in figure 4. The point denoted as C-2 represents data from a TriAlpha FRC, clearly better than the tokamak results. Whether the same improvement occurs in FRCs at higher ion temperatures needs to be tested.

There are reasons to believe this improvement will occur. First, the main culprit expected[25] to cause anomalous energy transport in FRCs is called the lower-hybrid drift instability (LHDI), predicted to create mm- to cm-scale turbulence that increases transport. The LHDI growth rate, γ_{LH}, is the ratio of the electron drift speed to the ion thermal velocity. As ions get hotter and the plasma denser, γ_{LH} gets smaller and the LHDI should become less important.

Secondly, Rostoker[26] and others[27] noted that hot ions and runaway electrons in *tokamaks* had far better confinement than thermal electrons. The reasons proposed for the large improvement was lower collisionality and less scattering by fluctuations because, like large ships in a choppy sea, the large gyro-radii of these energetic particles made them less susceptible to small-scale fluctuations.

2.3. Plasma current drive and plasma heating

RMF_e was proposed to drive current in the plasma, not to heat it to fusion-relevant temperatures. The current-drive mechanism was explained as being of 2nd order, specifically, the time-varying RMF_e magnetic field (in the r and ϕ directions) created a z-directed electric field (along **B**), hence a current in that direction, J_z. From the **J**x**B** term in the fluid momentum equation, J_z interacted with B_r, resulting in the desired azimuthal current $J\phi$.

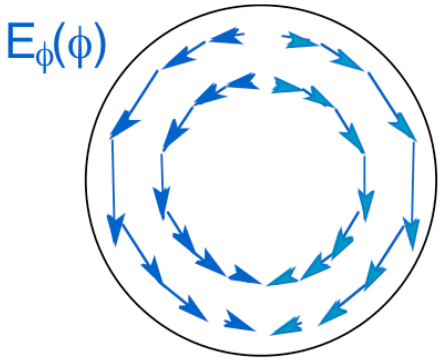

Figure 5. Snapshot of the azimuthal electric field in the FRC's midplane created by RMF_o. This field rotates with the RMF_o.

In contrast, RMF_o current drive is 1st order because of its B_z near the FRC's midplane. The time variation of that field creates an azimuthal electric field, $E\phi$, near the O-line magnetic null, figure 5, directly accelerating charged particles into betatron orbits near the null, figure 6a). More precisely, the trajectories are punctuated betatron orbits, separated by periods in cyclotron motion. As the particles are accelerated along the null, they gain then lose energy, figure 6b), because the (slowly rotating) $E\phi$ reverses direction halfway around. The more energetic the particles get, the further away from the null they can circulate. In the RMF_o's rotating frame, figure 6c), these punctuated betatron-orbit electrons form a crescent, hence move, on the average, with an azimuthal velocity equal to that of the RMF_o.[28]

In an FRC reactor, these current-carrying electrons will have very high peak energy, about 5 times greater than in D-T tokamak fusion reactors, consequently their collisionality will be more than 10x less. This contributes strongly to the high efficiency of RMF_o for driving current. Away from the O-line null, the more massive ions will carry an appreciable part of the current and diamagnetism will also provide a substantial part of the required current.

---

*Corresponding author, scohen@PPPL.gov

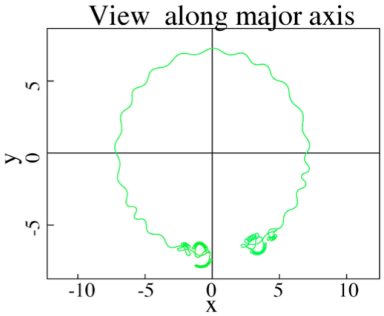

Figure 6a). Punctuated betatron orbit near the FRC midplane. At the start and end of the betatron segments, the orbit becomes cyclotron. (B_o = 20 kG, r_s = 10 cm, ω_{RMF}/ω_{ci} = 0.5)

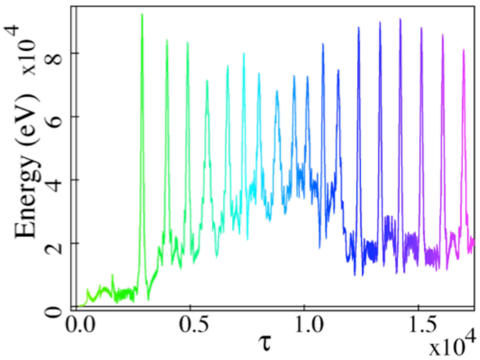

Figure 6b). As the electron moves against $E\phi$ it gains energy; as it moves with $E\phi$, it loses energy, resulting in the spikes in energy.

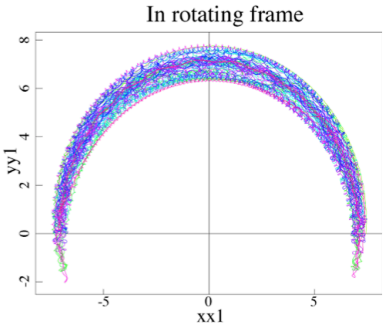

Figure 6c). In the frame rotating with the RMF_o, the punctuated betatron trajectory appears as a crescent, with the betatron segments "inside" the cyclotron segments.

Ion heating results from the same physical process, acceleration by $E\phi$, with an additional contribution from the RMF_o-created *z* and *r* electric fields. That the RMF_o frequency should not be far from the ion cyclotron frequency (at the FRC's center) to allow quasi-resonances, particularly at higher harmonics, is seen in figure 7b). Importantly, for both electron and ion heating, the non-uniformity of the FRC's magnetic field, especially the presence of nulls, causes orbits to lose track of the phase of the RMF, introducing stochasticity into the motion hence net energy gain.[29] Near Maxwellian distributions may develop, though usually the distributions are truncated at higher energy. Note that the required RMF_o strengths, to ~ 200 G, and frequencies, 0.3-3 MHz, to achieve ion energies of 100 keV are well within the capabilities of conventional RF equipment. Of course, improvements in RF amplifier efficiency and reduction of amplifier mass would provide important benefits.

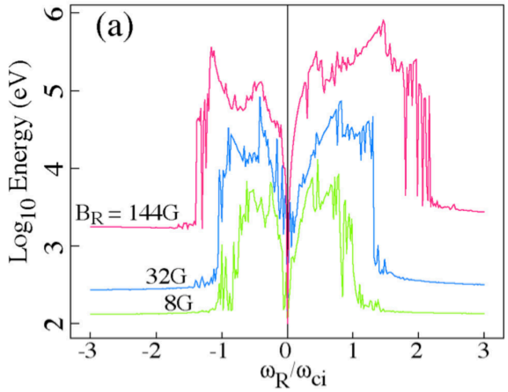

Figure 7a). Maximum ion energy versus RMF_o frequency for different RMF_o strengths in a 10-cm radius, 20-kG FRC.

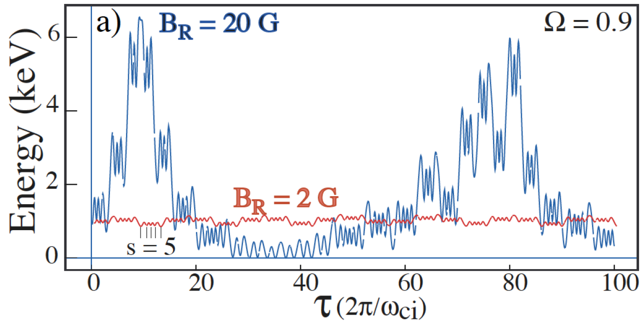

Figure 7b). Early time evolution of ion energy for two values of the RMF strength, 2 and 20 G. The quasi-resonances at higher harmonics, 3-5, are evident, as is the stochastic nature of the heating.

Having a small FRC, allowed because of the better energy confinement, makes RMF_o operation better. It improves the penetration of the RMF_o field to the FRC's null line where current drive is more efficient; it requires higher RMF_o frequency, which results in higher ion energies because $E\phi \propto \partial B/\partial t$. As we shall shortly see, other important benefits accrue, ones that result in far lower neutron wall load.

3. Fuel choice, neutron production, and power balance

The production of neutrons by fusion is particularly problematic for spacecraft propulsion. Neutrons cause damage and activation of nearby materials and structures, limiting their lifetime, necessitating maintenance, and increasing the mass needed for shielding. Neutrons are hard to "direct" hence may contribute little to the thrust required of a rocket engine. Having all the fusion products be charged particles solves these problems at the added cost of requiring higher plasma temperatures because of the lower fusion cross sections of the "advanced" *aneutronic* fuels. Of the two *aneutronic* fuels most commonly discussed, we choose D-^{3}He instead of p-^{11}B. The low energy release from p-^{11}B fusion, *plus* the lower fuel density possible at fixed magnetic

---

*Corresponding author, scohen@PPPL.gov

field (because of the higher nuclear charge) and the higher temperatures required, makes p-^{11}B a dubious choice. A penalty must be paid for selecting D-^{3}He. There are neutrons from one D-D fusion branch and possibly from the T fusion product of the other D-D fusion branch. Methods must be found to ameliorate these effects.

3.1. Reducing neutron wall load

A small FRC allows solutions to these problems. The surface-to-volume ratio scales as 1/radius. For a 25-cm radius FRC, a 32-fold improvement is obtained compared to an 8-m tokamak. Additionally, fusion products born in a small FRC will have their orbits pass through the cool SOL of the FRC where the electron drag is strong. By an "airbrake"-like effect, see figure 8a), fusion products which pass through the SOL even for a small fraction of their birth orbit, will rapidly cool, from 1 Mev to 100 keV, and their orbits will become cyclotron-like, lying fully in the SOL, figure 8b). PIC studies[30] of the slowing down indicate that this process will occur in under 10 ms, far quicker than the estimated 20-s T burn-up time. Once in the SOL, the T^+ will be exhausted out the nozzle with the cooler propellant, to be described in section 4. Only those neutrons produced by D-D fusion will remain a problem.

The third step in reducing neutron production is to increase the ratio of ^{3}He to D in the plasma.[31] This does reduce the power density approximately linearly but the percentage of power in neutrons quadratically.

From a neutron-production perspective, the net effect of these 3 measures should be in excess of a thousand-fold[32] reduction of neutron power flux to the first wall. The thickness of the neutron shielding, 100% ^{10}B, would be 10-30 cm, based on the duration of the mission and of the fusion-power production.

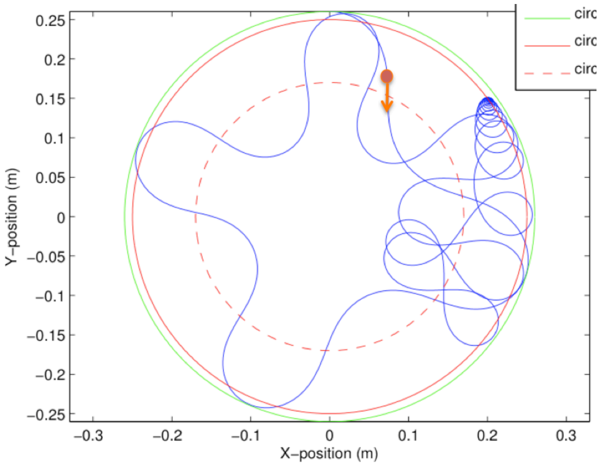

Figure 8a). T^+ trajectory projected on the midplane of an FRC. The T^+ slowing down by electron drag in the SOL is accelerated to show the transition of the orbit from betatron to figure-8 to cyclotron, the latter lying fully in the SOL, the region between the red and green circles.

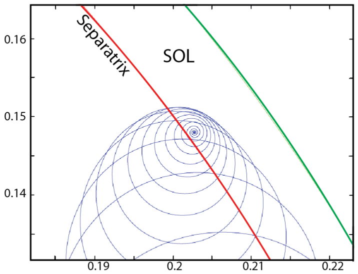

Figure 8b). Close-up view of the cyclotron segment of the T^+ orbit, showing that the orbit eventually lies fully in the SOL.[32]

3.2. Power balance and rocket subsystems

In this section we analyze a point design for a DFD rocket engine, focusing on power balance, to see if a consistent solution exists within the stability, energy confinement, and low radioactivity constraints described above. We begin by specifying the plasma density, ion and electron temperatures, plasma radius and elongation, and the external coils inner radius, r_c. The latter, determined by the thickness of the SOL and of the shielding, sets the plasma β through the Barnes relation, $< \beta > = 1 - x_s^2/2$, where $x_s = r_s/r_c$. Table 1 presents the results of our model with r_s =30 cm, E = 6, T_e = 30 keV, T_i = 100 keV, $n_e = 3\text{x}10^{20}$ m^{-3}, and a 2:1 ^{3}He to D ratio. Flat temperature and density profiles are assumed. From these, it is relatively straightforward to calculate β, fusion power, magnetic field strength, and plasma current, I_p. The next step is to calculate volumetric losses from radiation. Though Bremsstrahlung losses may also be calculated accurately, this is not the case for synchrotron losses because of plasma absorption and wall reflections. Our model assumes full emission from a 3-cm thick shell just inside the separatrix and no wall reflection. Further into the core the magnetic field is lower, hence the frequency lower; absorption of that emitted radiation occurs in the aforementioned shell. The Bremsstrahlung and synchrotron power will be absorbed in the neutron shielding. That energy is recovered with an efficiency of 60% by a Brayton cycle cooling system. Power flow into the gas box ionizes the propellant there. The energy cost is typically 50-100 eV/ion, with higher values required at lower densities. Of that power, 80-90% is deposited on the gas box walls and recovered by the Brayton cycle system. The power flows are depicted in

---

*Corresponding author, scohen@PPPL.gov

figure 9, which, for this DFD, is providing primarily thrust. If more electrical power is required for station keeping or communications, the thrust power can be diverted to generating electrical power. The distribution of masses is shown in figure 10. This assumes a conservative permitted neutron flux on the superconducting coils, below 10^{18} n/cm^2 and below 10^{-4} DPA, resulting in a 10-cm-thick ^{10}B shield, sufficient for 1 year at full power. Increasing the shielding thickness to 22 cm would increase the superconducting-coils lifetime to 13 years.

Table 1. Parameters for a 2-MW DFD rocket engine.

Parameter	DFD
r_s (m)	0.3
Elongation, E	6
B_a (T)	4.3
I_p (MA)	8.0
Ion species	D-^{3}He
^{3}He/D	2
n_e (m^{-3})	3 x10^{20}
T_e (keV)	30
T_i (keV)	100
$<\beta>$	0.84
P_{RMF} (MW)	0.5
ω_R (radians/s)	1.6x10^6
B_R/B_a	0.003
P_f (MW)	2.13
P_{synch} (MW)	0.7
P_{Bremss} (MW)	0.32
P_{GB} (MW)	0.1
${}_{classical}\tau_{Ei}/\tau_E$	2.7
s (T^+)	2.3
s ($^4He^{++}$)	2.2
S*/E	2.8
γ_{LH}	0.02
$\psi_{RMF\ penetration}$	34
Isp (s)	2.3x10^4
Thrust (N)	12.5
B_{nozzle} (T)	20
% power in neutrons	1.1
Wall load (MW/m^2)	2x10^{-3}

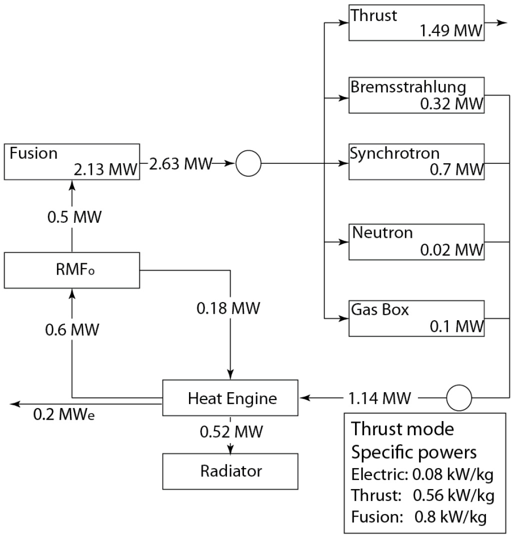

Figure 9. Power-flow diagram of a 2-MW DFD.

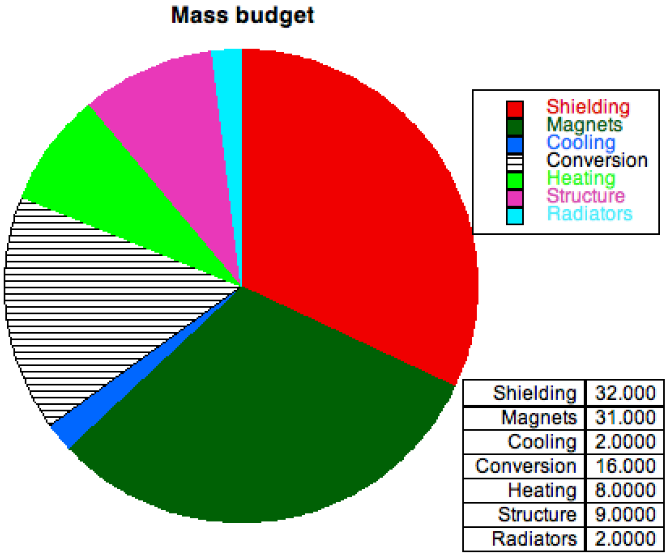

Shielding	32.000
Magnets	31.000
Cooling	2.0000
Conversion	16.000
Heating	8.0000
Structure	9.0000
Radiators	2.0000

Figure 10. Mass budget of the DFD engine.

We now examine the consistency of this design point with energy confinement, stability, and propulsion. The ratio of the classical confinement time, ${}_{classical}\tau_{Ei,}$ to the required energy confinement time is 2.7, consistent with the improvement in energy confinement seen by C-2 and PFRC-1. The two stability criteria are also satisfied: the LH micro-stability criterion, γ_{LH}, is < 1 and macro-stability criterion, S*/E, is less than 3. One further criterion[10] worth mentioning, named $\psi_{RMF\ penetration}$, is that for RMF field to penetrate in the core of the FRC. This parameter was derived for RMF$_e$ not RMF$_o$, so its applicability is questionable. For RMF$_e$ $\psi_{RMF\ penetration}$ must be greater than 1 for penetration. For the DFD, this parameter is above 30, an encouraging margin in light of the possible lack of direct applicability.

---

*Corresponding author, scohen@PPPL.gov

The neutron wall load for this plasma is 2500x below that specified as acceptable in D-T tokamaks, a sizeable improvement. The amount of thrust power lost in the neutron channel is small, 1%, though could be lowered by increasing the ^{3}He/D ratio.

The I_{sp} predicted for the DFD depends on the propellant species and injection rate into the gas box. For Table 1 we have selected a low propellant injection rate, one that produces an I_{sp} above 2 x 10^4 s. For higher propellant flow, I_{sp} would drop and the power required in the gas box would increase along with the thrust, topics we describe in more detail in section 4.

A pictorial representation of the subsystems is shown in figure 11 and an artist's rendition of a DFD module is in figure 12.

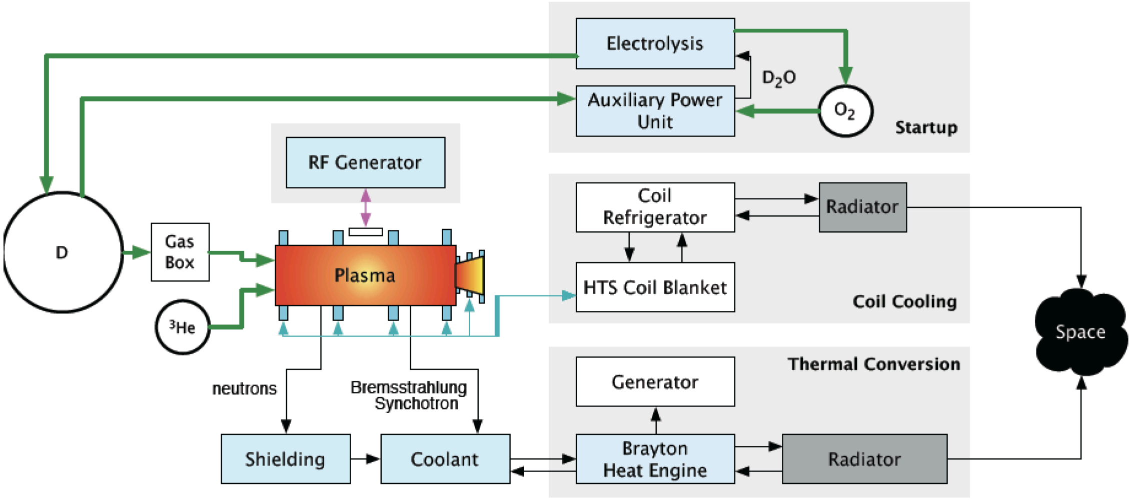

Figure 11. Block diagram of DFD major subsystems.

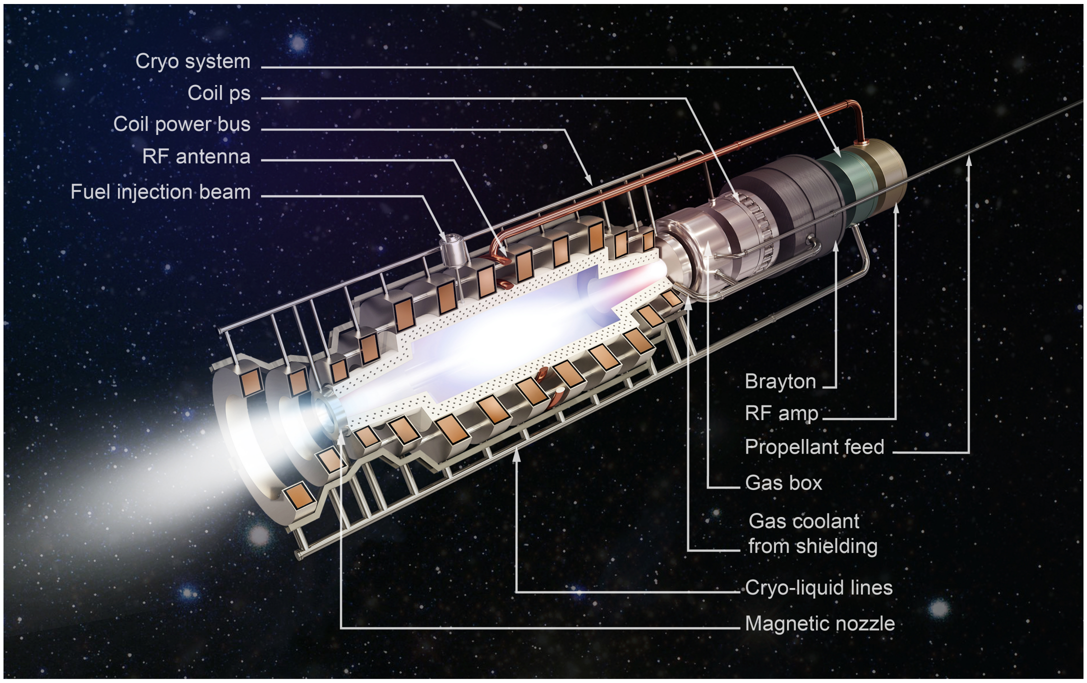

Figure 12. Artist's rendition of a 2-MW DFD module.

*Corresponding author, scohen@PPPL.gov

4. The scrape-off layer (SOL) and rocket exhaust

The SOL of the DFD is quite different than that of any other fusion device. In tokamaks, for example, the SOL is heated and populated by diffusive transport across the separatrix of both energy and particles. The heat transport into it is local, that is, described by Fick's law, by the local flux-surface-normal gradient in pressure. Because this diffusive transport is slow compared to the flow along the magnetic field, the SOL is onion-skin thin, δ_{SOL}, compared to the plasma's radius. For example, ITER's SOL is predicted to be ½-cm thick while the plasma outer radius at its midplane is 9 m, $^{\delta_{SOL}}/_{r_s} \cong 6x\ 10^{-4}$. It the DFD, the density profile of the SOL is determined by the orifice to the gas box and the field expansion between the gas box and the plasma midplane. For the DFD in Table 1, the SOL would be about 7 cm thick, $^{\delta_{SOL}}/_{r_s} > 0.2$. Energy is deposited across the entire SOL cross section by the large gyro-radii fusion products. Thus the DFD, the SOL + FRC, is more like a navel orange, with a very thick rind. The energy is deposited in the SOL directly from the fusion products *via* a non-local process and is predominantly transmitted to the electrons *via* fast-ion drag. The random thermal energy in the SOL electrons is transferred to the cool SOL ions through a double layer at the nozzle and *via* expansion downstream, thus being converted into directed flow.

Because of the relatively low temperature (< 100 eV) and high density (> $5\text{x}10^{19}$ m^{-3}) of the SOL, resulting in a collisional mean-free-path of the thermal (majority) electrons less than 50 cm, it is appropriate to use a fluid model for the SOL between the gas box and the nozzle. Results from one UEDGE[33] fluid-code simulation are shown in figure 13. In each, the gas box is 1-m long, at the far left, the electron heating occurs in the central 2 m, and the nozzle is located at z ~ 2 m. The inputs were P_i =1 MW of power and $\dot{m}$= 0.08 g/s of D_2 gas into the gas box. (The gas input is equivalent to a current, I_e = $\dot{m}N_A$ e/amu ~ 3.85 kA, where N_A is Avogadro's number and e the charge on an electron.) From $E_{max} = P_i/I_e$, one can then readily estimate the upper limit of ion energy to be 260 eV. As figure 13c) shows, only half that value is reached. The culprits are radiation and ionization losses and plasma energy brought to the gas box walls by plasma transport. The results of an extensive number of simulations are presented in figure 14, showing thrust reaching 10 N/MW.

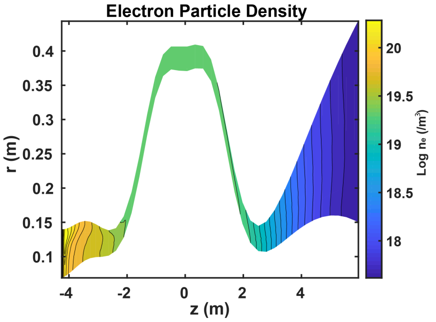

Figure 13a). Electron density, n_e, contours.

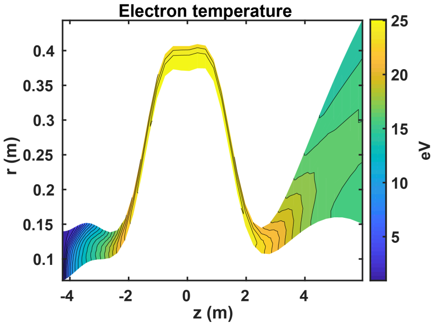

Figure 13b). Electron temperature, T_e, contours.

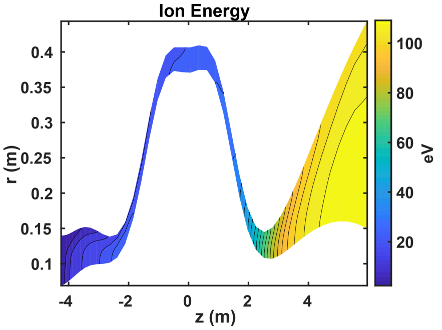

Figure 13c). Ion energy contours.

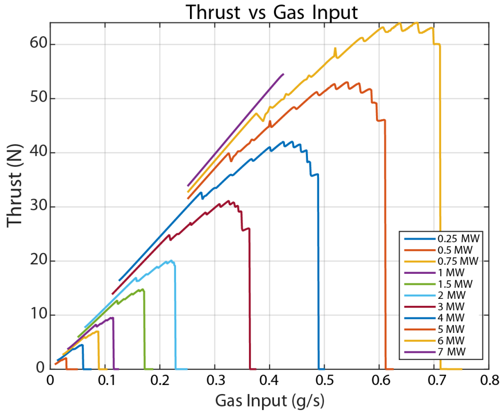

Figure 14a). Thrust *vs* gas feed for powers of 0.25 to 7 MW.

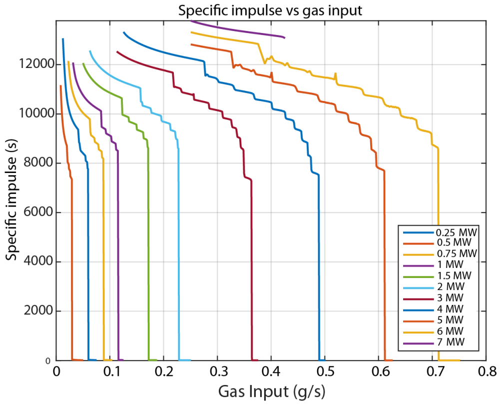

Figure 14b). Exhaust velocity *vs* gas feed for powers of 0.25 to 7 MW.

---

*Corresponding author, scohen@PPPL.gov

5. Missions

We describe two missions, one to place a 1-m telescope at 550 AU where it can use the sun as a gravitational lens to image exoplanets and the second to deliver a 1 MT payload to Alpha Centuri.

5.1. 550-AU mission

The 550-AU mission will carry a camera and other instruments to a distance of 550 AU (and beyond) from the Sun. At that distance, unique interstellar and solar system observations can be conducted. Using the Sun as a gravitational lens for imaging exoplanets is the one considered here. Conventional rocket technology would result in a 30-year transit to 550 AU; data collection would start in 2060. Using the Direct Fusion Drive (DFD), the transit time to 550 AU would be 13 years. Even accounting for development time, data collection will start 15 years earlier than with conventional technology, in 2045 rather than 2060. In transit and on arrival, the DFD would provide a megawatt of power for science, communication, and station-keeping. Furthermore, DFD allows a much smaller launch vehicle to be used, reducing mission costs substantially.

The mission objectives include the objectives of the Innovative Interstellar[34] and the 550 AU mission.[35,36] One instrument is an infrared telescope capable of looking back toward the Sun to assess the solar system dust that causes IR extinction as we look outward from Earth. It was too heavy for the Innovative Interstellar Explorer mission. The instruments are given in Table 2. The Exoplanet Imaging instrument would be a 1-m telescope with a large focal plane with a 0.4° field-of-view. The baseline communications system is a 40-GHz, Ka-band system with a 4-m-diameter transmit dish and 500-kW power. The data rates as a function of distance are shown in figure 15, sufficient to return a 1080p HDTV image every 6 seconds. (A 1-μ laser could increase the data rates 100-fold.)

Table 2. Instrument packages.[37] The power is that necessary to operate the instrument, not for communications.

Acronym	Instrument	Mass (kg)	Power (W)	Data rate (bps)
MAG	Magnetometer	8.81	5.30	130.00
PWS	Plasma wave sensor	10.00	1.60	65.00
PLS	Plasma parameters	2.00	2.30	10.00
EPS	Energetic particle spectrometer	1.50	2.50	10.00
CRS-ACR/GCR	Cosmic-ray spectrometer: anomalous and galactic cosmic rays	3.50	2.50	5.00
CRS-LoZCR	Cosmic-ray spectrometer: electrons/positrons, protons, helium	2.30	2.00	3.00
CDS	Cosmic dust sensor	1.75	5.00	0.05
NAI	Neutral atom detector	2.50	4.00	1.00
ENA	Energetic neutral atom imager	2.50	4.00	1.00
LAD	Lyman-alpha detector	0.30	0.20	1.00
EXOI	Exoplanet Imager	20	100	3×10^6
IRD	Infrared camera for solar system dust	10	100	3×10^6
	Total resources	35.16	229.40	6×10^6

The exoplanet telescope focus extends semi-infinitely. A 1-meter telescope, with coronagraph components, could resolve 3-km features on a planet 30 parsecs away. The light from the exoplanet appears as a ring around the sun, whose disc of light is blocked. There are many complexities[38] to the data analysis: pointing; focal properties of the sun are different in the radial and azimuthal directions; signal to noise; the exoplanet moves across the field of view; *etc*. The spacecraft is translatable perpendicular to the focal length vector to produce an image.

High-spectral-resolution spectroscopic data is available for every 3-km pixel. The unprecedented spectral resolution allows LANDSAT-like characterization of the exoplanet surface. Geological and material features of the 3km x 3km areas can be determined. Weather patterns can be tracked in real time. If the target exoplanet were Earth, the extent of industrial and agricultural use would be available for each 3km x 3km area.

---

*Corresponding author, scohen@PPPL.gov

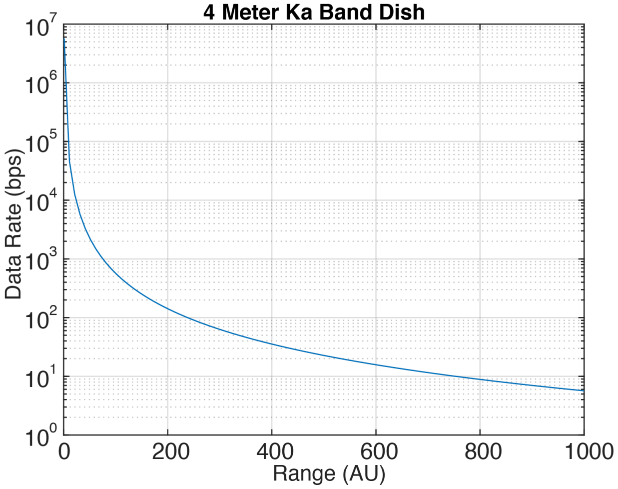

Figure 15. Data rate for a Ka-band communication system.

Figure 16. Example of what the telescope might be capable of resolving from 30 parsecs.[39]

A list of select spacecraft specifications is shown in Table 3. The fuel mass does not include that for the outgoing spiral. The "efficiency" is the fraction of power that goes into thrust; the fuel "tank fraction" is the ratio of its mass to that of the fuel. Once the spacecraft departs from Earth, it takes 13 years to reach 550 AU. The same spacecraft could be put into solar orbit at 550 AU in 18 years. The additional time is due to deceleration. Orbiting at 550 AU could not be done with a solar sail or laser light sail.

Launch windows for gravity-assisted missions can be decades apart while a direct flight does not require any particular launch window since it does not employ any flybys of the planets. It can be launched as soon as it is ready. Figure 17 shows a transfer (flyby) trajectory. The Earth departure spiral requires 400 kg of fuel from an ISS orbit and is shown in Figure 18. The spacecraft total mass of 5282 kg is low enough to be launched on any currently available launcher, as shown in Table 4. The spacecraft is in the inner radiation belt for 11.7 days.

Achieving the spacecraft performance values listed in Table 3 will be challenging. The specific impulse corresponds to 2.6 keV deuterons. In the lab[40] magnetic nozzles have produced only ~100 eV ions, though at considerably lower power (density) than the DFD. Higher I_{sp} studies would require kinetic codes rather than fluid ones because of the reduced collisionality.

Table 3. Select spacecraft specifications for the 550 AU flyby mission.

Parameter	**Value**	**Units**
Final position	555.6	AU
Final velocity	479.1	km/s
Final time	13.0	yr
Fuel	3217.6	kg
Mass Total	5282.	kg
Mass Engine	1700.	kg
Mass Payload	300.	kg
Exhaust Velocity	510.	km/s
Power	1.7	MW
Thrust	4.0	N
Specific power	1.0	kW/kg
Efficiency	0.30	
Tank fraction	0.02	

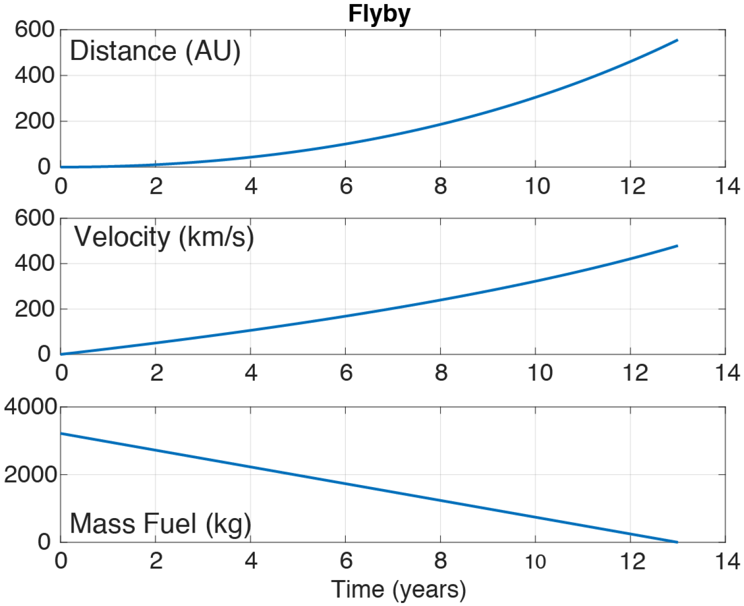

Figure 17. Flyby trajectory parameters.[41]

*Corresponding author, scohen@PPPL.gov

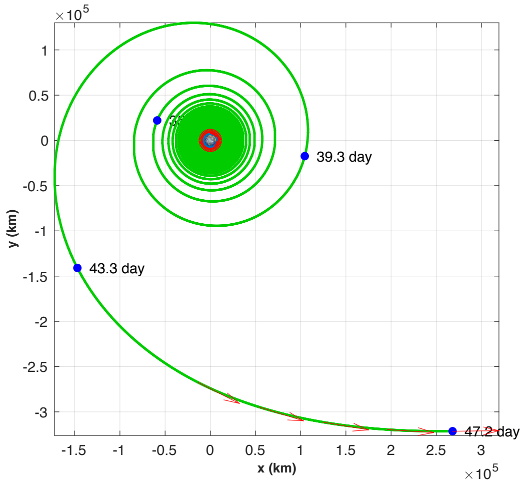

Figure 18. Earth departure spiral.[41]

Table 4. Launch vehicles to put spacecraft into LEO.

Family	Launch Vehicle	LEO (kg)	ISS (kg)
Atlas	401	9800	8910
	411	12030	10260
	431	15260	13250
	501	8210	7540
	511	11000	10160
	531	15530	14480
	551	18850	17720
Delta IV	Medium	9190	8510
	Medium+ (4.2)	12900	12000
	Medium+ (5.2)	11060	10220
	Medium+ (5.4)	13730	12820
	Heavy	28370	25980
Falcon 9	Block 1	9000	8500
	Block 1.1	13150	12420

5.1.1. Spacecraft Design

The spacecraft design is shown in figure 19. The 4-m-dia Ka-band high gain antenna dominates the spacecraft. A single DFD engine is used. While a second engine would give the system some redundancy, it may be better just to fly two spacecraft. For other missions, multiple engine modules offer strong benefits, noted later. The solar panels are for the spacecraft LEO checkout phase. The deuterium (propellant) tank is the larger of the two and is cryogenic. It has a cryo-cooler to recirculate boil-off. Helium-3 is stored as a gas in the smaller tank. The antenna, small blue vertical panels) and radiators (large black horizontal panels) are deployable.

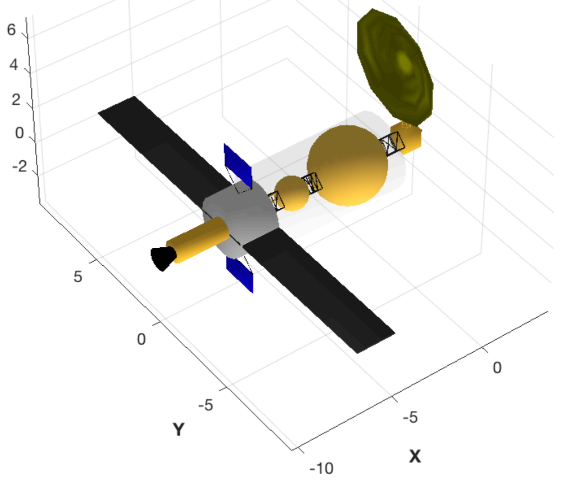

Figure 19. Spacecraft design. The large tank is for liquid D, the smaller tank is for gaseous helium-3.

5.2. An interstellar mission

Interstellar missions require much longer burn durations, and higher I_{sp} and specific power than the 550 AU mission. Figure 20 shows the rendezvous distance as a function of specific power and thrust for a 325-year-duration mission. The power is fixed at 100 MW. The exhaust velocity is found by solving the power equation,

$$u_e = \frac{2\eta P}{T} \tag{1}$$

where η is the power to thrust efficiency, ~ 0.3. Figure 21 shows the same but for a flyby. The maximum distance at each specific power is achieved for different thrust levels. At low specific powers, higher thrusts send the spacecraft further. This is not true at high specific powers. At a specific power, the maximum distance is achieved with 4 N thrust, not 8 N. There will be an optimal thrust for every duration and specific power. The exhaust velocity assumed is a sizeable fraction of that of the full energy of the fusion products. The distance as a function of time for intercept is

$$d = u_e\left[\left(\tau - \frac{m_s}{\dot{m}}\right) log\left(1 - \frac{\dot{m}}{m_s}\tau\right)(1 - \frac{m}{m_s}) - \left(t_s - \frac{m_0}{\dot{m}}\right) log\left(1 - \frac{\dot{m}}{m_s}t_s\right) + t_s - \tau\right] + v_s\tau \tag{2}$$

---

*Corresponding author, scohen@PPPL.gov

where m_s is the mass at switch time, $\dot{m}$ is the mass flow rate, u_e is the propellant exhaust velocity, $\tau = t_f - t_s$, $m_s = m_0 - \dot{m}t_s$, and v_s is the velocity at switch time,

$$v_s = u_e log\left(1 - \frac{\dot{m}}{m_0}t_s\right) \tag{3}$$

The switch time is found from the quadratic equation

$$t_s^2 - 2\gamma t_s + \gamma t_f = 0 \tag{4}$$

where $\gamma = \frac{m_0}{\dot{m}}$. The solution for t_s that is less than t_f is the correct solution.

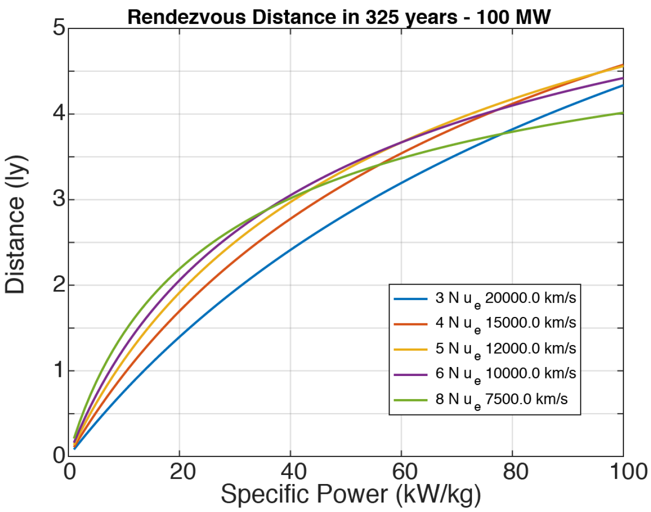

Figure 20. Rendezvous distance in 325 years for different thrusts and specific powers.[41]

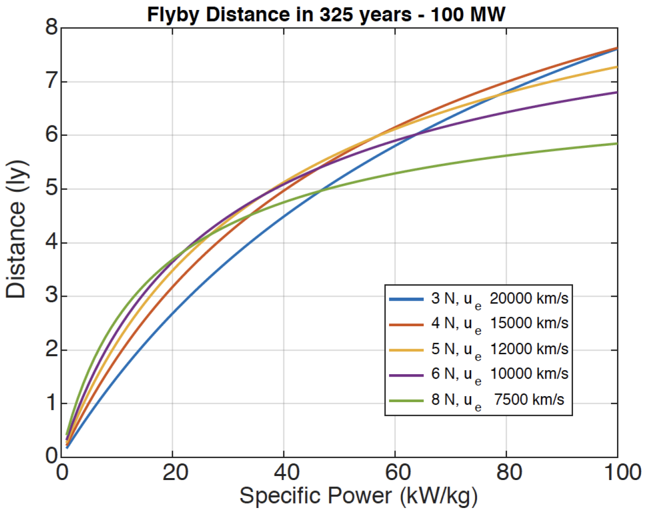

Figure 21. Flyby distance after 325 years of constant thrust.[41]

Entry into the star system is similar to entry into a planetary orbit within the solar system. The approach geometry is shown in figure 22. The final orbit adjust maneuver is shown in figure 23. By the time such a mission is launched, accurate information about planetary orbits should be available so that the maneuvers can be planned in advance. Once in orbit the spacecraft would have up to 100 MW of power to transmit data back to earth. The data rate from interstellar space using a 95 MW laser transmitter is shown in figure 24.

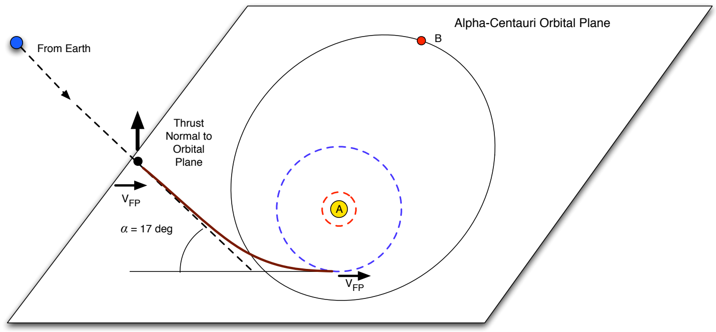

Figure 22. Approach to Alpha-Centuri.[41]

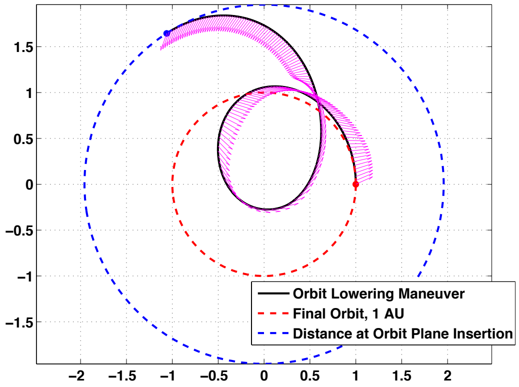

Figure 23. Final orbit adjust.[41]

If the engine burns for 500 years it could go further, reaching Alpha-Centauri, with specific power of 25 kW/kg, in 500 years. This is shown in figure 25 for a rendezvous. Currently our best estimates of attainable specific power are from 0.3 to 1.5 kW/kg, woefully inadequate for these missions. To achieve the high numbers in these plots would require a number of revolutionary improvements, such as:

---

*Corresponding author, scohen@PPPL.gov

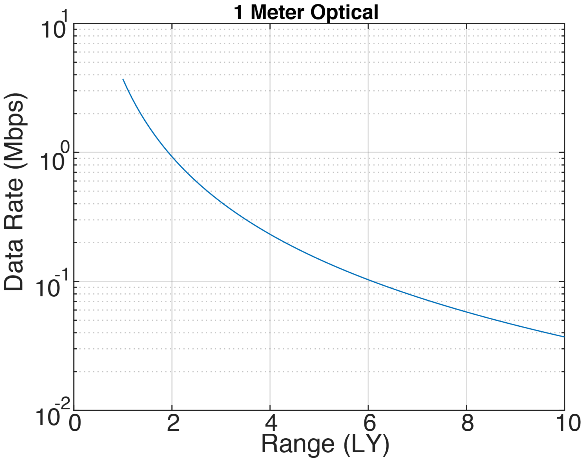

Figure 24. Data rate from interstellar space for a 95-MW transmitter.

- Replace the Brayton cycle heat engine with a method of direct conversion from x-rays and waste heat to radio-frequency power. Direct conversion of heat to electricity is done now but is only about 5% efficient. Direct conversion of x-rays is done in x-ray machines but the efficiency is very low.
- Use DFD staged modules - consume then jettison. This is similar to chemical rockets today, with the significant difference that all remaining DFD modules provide thrust until they and their propellant tanks are jettisoned. The performance improves with the logarithm of the mass of the extra stages.[42] Employing 100 DFD units, a flyby of Alpha-Centuri within 350 years is then achievable at a specific power of 5 kW/kg, an improvement compared to requiring 30 kW/kg for a single 100 MW DFD, as depicted in figure 21.
- Make superconductors that can last 300-500 years in the face of neutron bombardment.
- Make superconductors that retain their superconducting properties at higher temperatures, to reduce the need for cryo-coolers.
- Lower mass structures.
- Increasing ^{3}He supply, perhaps by T-suppressed D-D fusion reactors. The currently available ^{3}He supply is (x1000) inadequate for a 100-MW-power, 300-year mission.
- Closed cycle method for recycling propellant/coolant during electrical power generation mode of operation, to reduce the system mass.

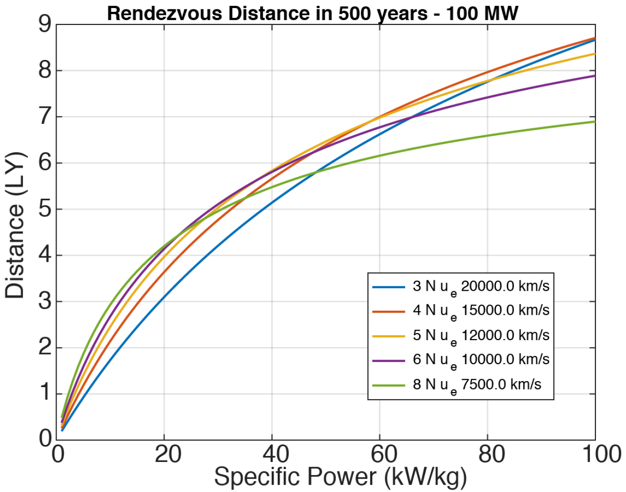

Figure 25. Rendezvous distance after 500 years.[41]

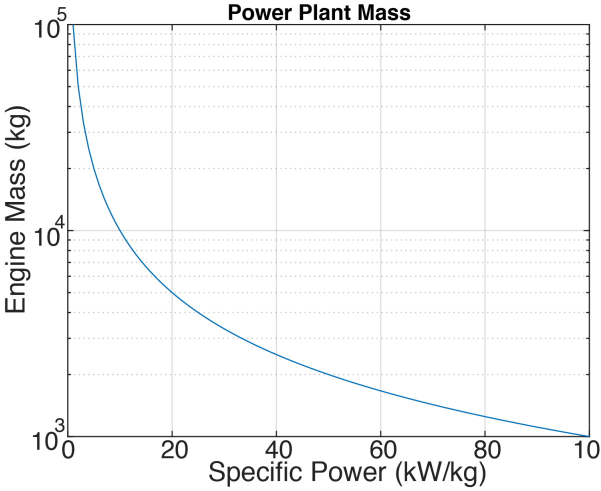

Figure 26. Mass of a 100 MW power plant as a function of specific power.[41]

Figures 27 and 28 show example trajectories for the 325-year rendezvous and flyby missions. The parameters for these cases are: a constant thrust of 4 N; a specific power of 100 kW/kg; engine power of 160 MW; and an exhaust velocity of 24,000 km/s. Note the switch time is beyond the halfway point as the spacecraft continues to become less massive. Using multiple engine modules, and jettisoning them and empty propellant tanks along the way, could reduce the required specific power a factor of 10 while keeping the trip duration and payload the same. These jettisoned modules could act as relay stations for communications, increasing the data rates enourmously.

---

*Corresponding author, scohen@PPPL.gov

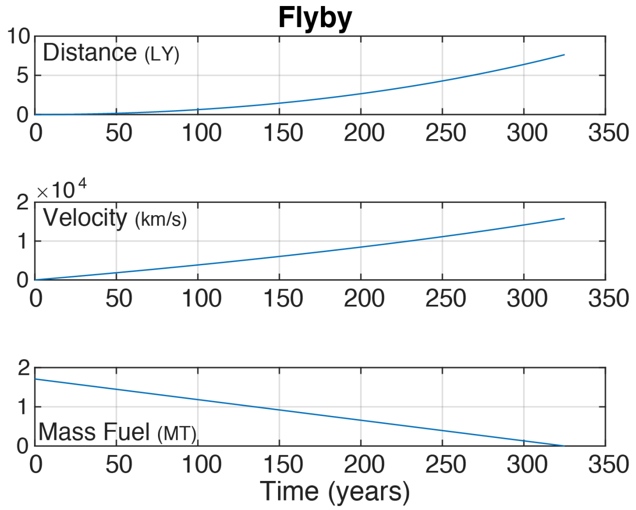

Figure 27. Sample flyby trajectory for T = 4 N.[41]

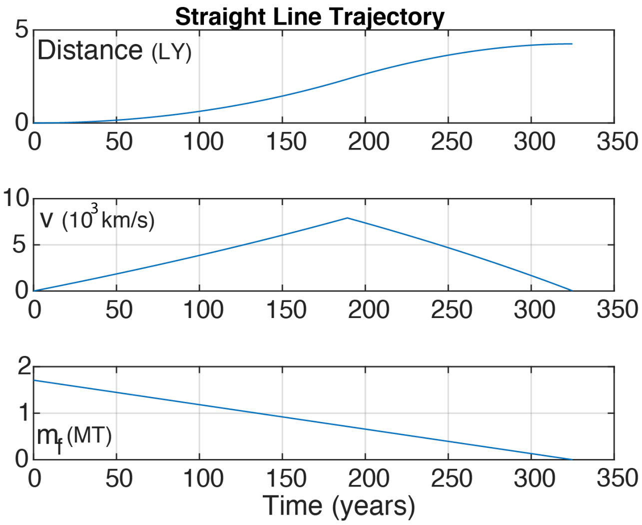

Figure 28. Sample rendezvous trajectory for T = 4 N.[41]

6. Summary

The physics basis for low-radioactivity, FRC fusion reactors has steadily grown over the last two decades, with innovative contributions from theory, modeling, and experiments. Importantly, stability limits, once thought to be a major issue, have been exceeded by a factor of 10^5 and energy confinement quality, seen in experiments and measured by the ratio of β to plasma thermal conductivity χ, is a factor of 10 better than in the mainline fusion reactor designs. Scaling predictions to hotter FRC plasmas is favorable. More recently, attention has been given to technical and engineering aspects, such as reducing the weight of subsystems, increasing electrical efficiency, and identifying components with high resistance to radiation damage.

From this foundation, we extrapolate to a Direct Fusion Drive rocket engine that would permit high scientific-return interstellar research missions in the 2030 time frame, provided advances are made in achieving fusion and producing the predicted thrusts and specific impulse levels. A DFD-powered spacecraft could be used for the 550-AU gravitational lensing mission. An Alpha Centauri flyby and orbital mission would require a ten-fold increase in mission duration and place far more difficult demands on the technical components. DFD has the potential to reduce the cost and increase the scientific return for most solar system robotic missions and human missions to nearby planets.

The paper illustrates, once again, the critical relationship between specific power and mission performance. The current estimated DFD specific powers are between 0.3 and 1.5 kW/kg. Far higher specific powers are desired for missions to other star systems, ones that will also require much better methods of recycling waste energy and components that are far less sensitive to neutron irradiation.

Near-term work includes the completion of the PFRC-2 ion heating experiment, detailed mission analysis, and subsystem designs for the engine components. Design work on higher efficiency RF heating systems and on superconducting magnets is underway. Design of PFRC-3 will begin once the ion heating experiments are complete. This will be about 50% larger than PFRC-2 and aims at higher plasma temperatures and pressures. The succeeding facility, the PFRC-4, is aimed at demonstrating fusion power generation with D-^{3}He. Additional work will be done on the integration issues of multiple engine modules, including the effect of one engine's field on another. A critical point is that the engineering challenges in the DFD design, though large, are greatly reduced, compared to all previous fusion rocket engine concepts, because of its small, clean, steady-state, and high-β modular nature. The DFD design allows ambitious missions throughout and outside the solar system.

Direct Fusion Drive has the potential to revolutionize space exploration. Near term research and development aim to move the technology to operational status by 2030.

This work was supported by the US Department of Energy Contract No. DE-AC02-76-CHO-3073 and NASA grant NNX16AK28G.

References:

---

[1] N. R. Schulze, "Fusion Energy for Space Missions in the Twenty-First Century," Technical Memorandum 4298, National Aeronautics and Space Administration (Aug. 1991).

[2] J.A. Angelo and D. Buden, “Space Nuclear Power,” Orbit Book Company, Malabar, FL, (1985).

[3] C. Williams, S. Borowski, L. Dudzinski, and A. Juhasz, “Realizing 2001: A Space Odyssey: Piloted Spherical Torus Nuclear Fusion Propulsion,” Tech. Rep. NASA/TM 2005-213559, NASA Glenn Research Center, (2005).

[4] N. Gorelenkov, L. Zakharov, P. Bhatta, and M. Paluszek, “Magnetic Fusion Engine,” 43rd AIAA/ASME/ SAE/ASEE Joint Propulsion Conference (2007).

[5] F. Romanelli, C. Brunob, and G. Regnolia, “Assessment of Open Magnetic Fusion for Space Propulsion,” Tech. Rep. 18853/05/NL/MV, The European Space Research and Technology Centre, (2005).

[6] E. Teller, A.J. Glass, T.K. Fowler, *et al.*, “Space propulsion by fusion in a magnetic dipole,” Fusion Technology **22**, 81 (1992).

[7] J. Slough, D. Kirtley, A. Pancotti, *et al.*, “A Magneto-Inertial Fusion Driven Rocket”, ICOPS 1P-125 (2012).

[8] K. Miller, J. Slough, and A. Hoffman “An overview of the Star Thrust experiment,” AIP Conference Proceedings 420, 1352 (1998).

[9] H.A. Blevin and P.C. Thonemann, “Plasma confinement using alternating magnetic field,” Nucl. Fusion: 1962 Supplement, Part 1, 55 (1962).

[10] W.N. Hugrass and R.C. Grimm, “A numerical study of the generation of an azimuthal current in a plasma cylinder using transverse rotating magnetic field,” J. Plasma Physics **26**, 455 (1981).

[11] Y.S. Razin, G. Pajer, M. Breton, *et al.*, “A direct fusion drive for rocket propulsion,” Acta Astronautica **105**, 145 (2014).

[12] S.A. Cohen and R.D. Milroy, “Maintaining the closed magnetic-field-line topology of a field-reversed configuration with the addition of static transverse magnetic fields,” Phys. Plasmas **7**, 2539 (2000).

[13] M.N. Rosenbluth and M.N. Bussac, “MHD theory of the spheromak,” Nucl. Fusion **19**, 489 (1979).

[14] J. Friedberg, *Ideal MHD*, Cambridge University Press (2014).

[15] A. Ishida, H. Momota, and L. C. Steinhauer, “Variational formulation for a multifluid flowing plasma with application to the internal tilt mode of a field-reversed configuration,” Phys. Fluids **31**, 3024 (1988).

[16] L.C. Steinhauer, “Review of field-reversed configurations,” Phys. Plasmas **18**, 070501 (2011).

[17] I.R. Jones, “A review of rotating magnetic field current drive and the operation of the rotamak as a field-reversed configuration and a spherical tokamak,” Phys. Plasmas **6**, 1950 (1999).

[18] Y. Petrov, X. Yang, Y.Wang, and T-S Huang, “Experiments on rotamak plasma equilibrium and shape control,” Phys. Plasmas **17**, 0112506 (2010).

[19] S.A. Cohen, B. Berlinger, C. Brunkhorst, *et al.*, “Formation of collisionless high-β plasmas by odd-parity rotating magnetic fields,” Phys. Rev. Lett. **98**, 145002 (2007).

[20] H.Y. Guo, M.W. Binderbauer, T. Tajima, *et al.,* “Achieving a long-lived high-beta plasma state by energetic beam injection,” Nature Communications, |6:6897| DOI: 10.1038/ncomms7897 (2015).

[21] Private communication, E. Lieberman.

[22] H.Y. Guo, A.L. Hoffman, and L.C. Steinhauer, “Observations of improved confinement in field reversed configurations sustained by antisymmetric rotating magnetic fields,” Phys. Plasmas **12**, 062507 (2005).

[23] J. Sheffield, “Physics requirements for an attractive magnetic fusion reactor,” Nucl. Fusion **25**, 1733 (1985).

[24] J. Wesson, *Tokamaks*, Oxford University Press, 4th edition, Oxford (2011).

[25] N.A. Krall and P.C. Liewer, “Low frequency instabilities in magnetic pulses,” Phys.Rev. A. **4**, 2094 (1971).

[26] N. Rostoker and A. Qerushi, “Classical transport in a field reversed configuration,” Plasma Physics Reports, **29**, 626 (2003).

[27] C.W. Barnes, J.M. Stavely Jr. and J.D. Strachan, “High-energy runaway electron transport deduced from photonuclear activation of the PLT limiter”, Nucl. Fusion 21, 1469 (1981).

[28] A.H. Glasser and S.A. Cohen, “Ion and electron acceleration in the field-reversed configuration with an odd-parity rotating magnetic field,” Phys. Plasmas **9**, 2093 (2002).

*Corresponding author, scohen@PPPL.gov

---

[29] S.A. Cohen, A.S. Landsman, and A.H. Glasser, “Stochastic ion heating in a field-reversed configuration by rotating magnetic fields,” Phys. Plasmas **14**, 072508 ((2007).

[30] E.S. Evans, *et al.,* “Particle-in-cell studies of fast-ion slowing-down rates in cool tenuous magnetized plasmas,” to be submitted to Phys. Plasmas (2017).

[31] J.F. Santarius, “Role of advanced-fuel and innovative-concept fusion in the nuclear renaissance,” Bull. Amer. Phys. Soc. **51**, 147 (2006).

[32] S.A. Cohen, M. Chu-Cheong, R. Feder, *et al., “*Reducing Neutron Emission from Small Fusion Rocket Engines,” IAC 2015, October, 2015, Jerusalem, Israel.

[33] T. Rognlien, J.L. Milovich, M.E. Rensink, and G.D. Porter, “The UEDGE Code”, J. Nucl. Mat., **196–198**, 347 **(**1992**).**

[34] R.L. McNutt Jr, R.E. Gold , T. Krimigis, *et al.,* “Innovative interstellar explorer”, *Physics of the Inner Heliosheath*, CP858, 2006.

[35] L. Alkalai, N. Arora, M. Shao, *et al.,* “Mission to the Solar Gravity Lens Focus: Natural Highground for Imaging Earth-like Exoplanets”, Planetary Science Vision 2050 Workshop, No. 8203, (2017).

[36] Paul Gilster, “The FOCAL Mission: To the Sun's Gravity Lens”, http://www.centauri-dreams.org, “Centauri Dreams Imagining and Planning Interstellar Exploration,” (2006).

[37] McNutt, R.L., Gold, R.E. Krimis, S.M., *et al.*, “Innovative Interstellar Explorer,” Proc. Workshop on Innovative Systems Concepts, The Netherlands, (2006) and McNutt, R.L., Gold, R.E. Krimis, S.M., *et al.*, “Innovative Interstellar Explorer,” *Physics of the Inner Heliosheath*, J. Heerikhuisen *et al.,* ed., Am. Inst. Phys. 978-0-7354-0355-0/06 (2006)

[38] G.A. Landis, “Mission to the gravitational focus of the sun: A critical analysis,” arxiv.org/abs/1604.06351

[39] E. Stone, L. Alkalai, L. Friedman, *et al.,* “Science and Enabling Technologies for the Exploration of the Interstellar Medium: Final Report,” Science and Enabling Technologies to Explore the Interstellar Medium conference, (2014). http://kiss.caltech.edu/new_website/programs/Final%20KISS%20ISM%20Report.pdf

[40] X. Sun, S.A. Cohen, E.A. Scime, and M. Miah, “On-axis parallel ion speeds near mechanical and magnetic apertures in a helicon plasma device,” Phys. Plasmas **12**, 103509 (2005).

[41] Simulations performed with *The Spacraft Control Toolbox,* see Paluszek, M., Thomas, S. *et al.*, “The Spacecraft Control Toolbox for MATLAB v2016.1,” Princeton Satellite Systems, 2016.

[42] H.S. Seifert and K. Brown (editors), *Ballistic missile and space vehicle systems*, New York Wiley, (1961).